ADVANCED FUNCTIONAL MATERIALS
www.afm-journal.de

Microphase Separation-Driven Sequential Self-Folding of Nanocomposite Hydrogel/Elastomer Actuators

*Jiayu Zhao and Jinhye Bae**

Untethered stimuli-responsive soft materials with programmed sequential self-folding are of great interest due to their ability to achieve task-specific shape transformation with complex final configuration. Here, reversible and sequential self-folding soft actuators are demonstrated by utilizing a temperature-responsive nanocomposite hydrogel with different folding speeds but the same chemical composition. By varying the UV light intensity during the photo-crosslinking of the nanocomposite hydrogel, different types of microstructures can be realized via phase separation mechanisms, which allow to control the folding speeds. The self-folding structures are fabricated by integrating two dissimilar materials (i.e., a nanocomposite hydrogel and an elastomer) into hinge-based bilayer structures via extrusion-based 3D printing. It has been demonstrated that the folding kinetics can be accelerated by more than one order of magnitude due to the phase-separated microstructure formed by the relatively weaker UV intensity (≈10 mW cm^{-2}) compared to the one formed by stronger UV intensity (≈100 mW cm^{-2}). 3D structures with sequential self-folding capabilities are realized by prescribing actuation speeds and folding angles to specific hinges of the nanocomposite hydrogel. Sequential folding box and self-locking latch structures are fabricated to demonstrate the ability to capture and hold objects underwater.

1. Introduction

Self-folding in response to environmental cues can be found everywhere in nature, with examples found in plant leaves,[1] insect wings,[2] and proteins.[3] Folding is capable of large deformation, complex shapes, and scalable sizes, making it appealing in a wide range of applications including robotics,[4] healthcare,[5] and electronic devices.[6] Structural inhomogeneity has been introduced into the material systems to create artificial self-folding structures that can automatically fold from a 2D sheet to a 3D object in response to external stimuli.[7] Specifically, origami-based design principles have been widely employed in various material systems such as elastomers,[6] shape memory polymers,[8] liquid crystal elastomers,[9] and hydrogels to create self-folding structures on demand by applying external stimuli,[10] where active hinges are patterned on a passive substrate to localize the deformation and lead folding to occur. Among these, stimuli-responsive hydrogels are of particular interest due to their ability to respond to versatile stimuli such as light,[11–13] humidity,[14] pH,[15] temperature.[16] Hydrogels are crosslinked hydrophilic polymers which allow for absorbing large amounts of water. The ability to control and program these stimuli-responsive hydrogels to morph into arbitrary shapes and perform complex tasks is enabled by the recent advance in modeling,[17] computation,[18] and manufacturing.[19] However, most 3D structures realized by the self-folding of stimuli-responsive hydrogels either have limited structural complexity or are geometrically constrained.[20,21] This is attributable to its simultaneous folding which causes self-collision problems when the patterns are designed to be more complex.[22]

Sequential self-folding has received considerable attention since it allows us to achieve the desired complex final configurations by designating the folding order of each hinge.[23,24] Generally, there are three strategies to create sequential folding. The first approach is to chronological move or changes the external stimulus, as demonstrated by Dai et al. where sequential folding is achieved by manually moving the stimulus source (i.e., electron irradiation) to locally actuate the structure.[25] Felton et al. and Liu et al. reported the sequential folding of shape memory polymer sheets due to local shrinkage of the shape memory polymer through localized heating in chronological order by applying the external stimuli (i.e., current and light).[24,26,27] Similarly, Kotikian et al. incorporated two different types of liquid crystal elastomers with different nematic-to-isotropic temperatures into a hinge-based structure that can be actuated by changing the environmental temperature

J. Zhao, J. Bae
Department of NanoEngineering
University of California San Diego
La Jolla, CA 92093, USA
E-mail: j3bae@ucsd.edu
J. Bae
Chemical Engineering Program
University of California San Diego
La Jolla, CA 92093, USA
J. Bae
Material Science and Engineering Program
University of California San Diego
La Jolla, CA 92093, USA
J. Bae
Sustainable Power and Energy Center (SPEC)
University of California San Diego
La Jolla, CA 92093, USA

The ORCID identification number(s) for the author(s) of this article can be found under https://doi.org/10.1002/adfm.202200157.

DOI: 10.1002/adfm.202200157

in a prescribed order.[28] Controlled sequential actuation of hydrogel has been shown by Baker et al., where ionoprinting was employed to pattern iron and vanadium cations into the hydrogel, and by applying selective redox reactions, the hinge patterned with iron can be unfolded while other hinges with vanadium remain fold.[29] The second strategy is to initially use different materials with different folding speeds when subjected to the same stimulus. Mao et al. reported sequential self-folding structures fabricated by shape memory polymers with different compositions that possess different thermomechanical behaviors at a certain temperature.[30] Lee et al. achieved a controlled folding speed of the polymer sheet by varying the chemical composition of hinges that changed the degrees of transparency and thus heat absorption.[31] The third strategy is to vary the dimensions of the active materials. Liu et al. and Iwase et al. reported 3D microstructures by sequential self-folding enabled by changing the structural parameters (i.e., the thickness, length, and width) of the active hinges.[23,32] However, to our best knowledge, it has not been previously reported that sequential self-folding can be enabled by using a single active material without changes in chemical composition and structural design under a static external stimulus. The achievement of which could greatly simplify the fabrication processes. Therefore, we focused on varying the internal microstructure of a stimuli-responsive hydrogel-based active material through decomposition mechanisms instead of changing its chemical composition to tune its actuation speeds.

Phase separation in mixtures containing a polymer gives rise to a polymer-rich phase and a polymer-poor phase, which alternatively can be used as a tool to control the microstructure via different decomposition mechanisms.[33] This strategy has been employed to create versatile advanced materials with desired properties such as excellent mechanical properties,[34] and improved energy conversion efficiency.[35] In particular, photo-crosslinking induced phase separation has been explored, in which a homogeneous solution composed of reactive monomers or polymers undergoes phase separation induced by the increased degree of polymerization and/or crosslinking upon irradiation with light. Previous studies demonstrated that a wide variety of morphologies can be produced depending on the strength and spatial distribution of the competing effect of phase separation and photo-crosslinking.[36] Kimura et al. showed that phase separation via spinodal decomposition and nucleation-and-growth process in the mixture of polystyrene (PS) and methyl methacrylate monomer can be induced due to the deep and shallow quench resulting from high and low light intensity, respectively.[10] Similar light intensity dependence in phase separation also has been found during the photo-crosslinking process of PS and poly(vinyl methyl ether) mixture.[37] These studies suggest that the microstructure resulting from photo-crosslinking driven phase separation can be readily controlled by light intensity. Furthermore, phase separation has also been found as a promising way to manipulate microstructure in nanocomposite polymers. Self-assembly and selectively dispersion of nanoparticles (NPs) in polymer matrices due to the reaction-induced phase separation after polymerization and/or crosslinking have been demonstrated before, including the colloidal crystal of gold NPs formed in an amphiphilic physical gel,[38] and selectively localized graphite nanoplates at the interface of two polymer matrices.[39] Despite the recent advances, this strategy to control the spatial distribution of NPs in the stimuli-responsive hydrogels has not been utilized to tune their swelling/de-swelling kinetics thus their shape morphing kinetics.

Herein, we demonstrate the sequential and reversible self-folding of a hinge-based bilayer structure by controlling the microstructures of the active nanocomposite hydrogel hinges, consisting of ploy(*N*-isopropylacrylamide) (PNIPAM) and nanoclay (NC), via nucleation-and-growth during photo-crosslinking by a relatively weaker UV intensity (20 mW cm^{-2}). The formation of phase-separated microstructures allows us to tune the folding speed of the bilayer structures prepared without variation in chemical composition and structural design. PNIPAM is a temperature-responsive hydrogel that is known to possess a lower critical solution temperature (LCST) ranging from 30 to 50 °C.[40] NC is a 2D disc that has ≈25 nm diameter and ≈1 nm thickness, which serves as a rheological modifier. The origami-inspired hinge-based bilayer structure is fabricated by integrating the temperature-responsive NC-PNIPAM as active hinges and the inert elastomer polydimethylsiloxane (PDMS) as passive substrates via extrusion-based 3D printing. UV intensity-dependent phase separation is induced during the photo-crosslinking of NC-PNIPAM, yielding hydrogels with homogenous and heterogeneous microstructures by relatively stronger UV intensity (253 mW cm^{-2}, denoted as NC-PNIPAM (253)) and weaker UV intensity (20 mW cm^{-2}, denoted as NC-PNIPAM (20)), respectively. Upon immersion in water after curing, the strain-mismatch generated between the swellable NC-PNIPAM hinge and non-swellable PDMS substrate leads to form self-folding structures. Reversible self-folding is enabled by reversible swelling and de-swelling of the active hinge upon cooling and heating, respectively. Full range of folding angles is achieved by varying the geometry parameters of the hinges. Notably, we demonstrate that controllable folding speed can be realized using the NC-PNIPAM hydrogels that possess different microstructures yet have the same chemical composition and hinge dimensions. We further explore the ability to actuate the folding structures in sequence by assigning different folding angles and actuation speeds to individual NC-PNIPAM hinges. We anticipate that this tunable shape morphing kinetics encoded responsive materials will open a new avenue for designing and fabricating shape actuation and morphing of nanocomposite hydrogel-based systems that enable the next level of complex shapes and tasks.

2. Results and Discussion

The hinge-based bilayer structures are fabricated by extrusion-based 3D printing. PNIPAM is chosen as a material for temperature-responsive active hinges,[41] and PDMS is used as a non-responsive passive substrate owing to its flexibility, inertness, and non-swellable in water.[42] However, it has been challenging to integrate hydrophilic hydrogels with hydrophobic elastomers due to the distinctive differences in their chemical nature. Several surface modification strategies have been proposed including treating the PDMS surface with oxygen plasma and silane, or photoinitiator (i.e., benzophenone).[43,44] However,

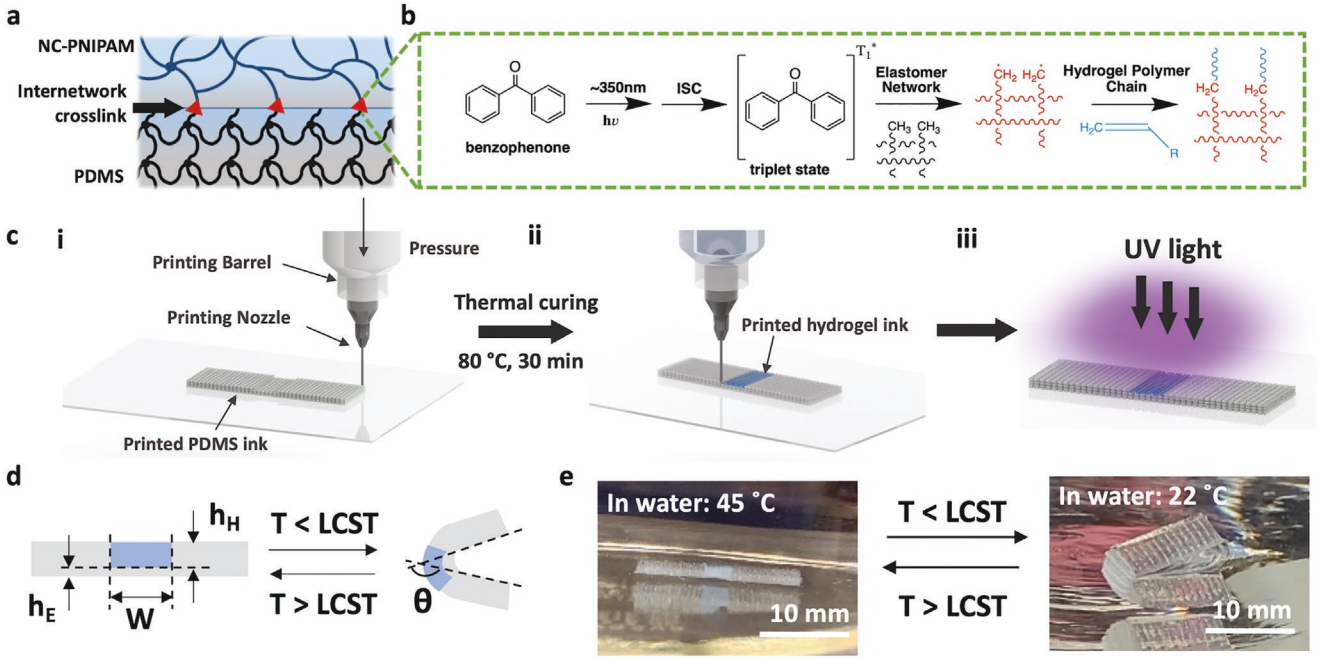

Figure 1. a) Schematic of the interface between NC-PNIPAM and PDMS; b) Adhesion mechanism between NC-PNIPAM and PDMS under UV irradiation; c) Schematic of the fabrication process: i, Extrusion-based 3D printing of PDMS substrate with hinge structure, followed by curing at 80 °C for 30 min in an oven; ii, The NC-PNIPAM hydrogel ink was printed on the cured PDMS substrate at the hinge part; iii, The printed structure was transferred to UV irradiation to photo-crosslink the NC-PNIPAM as well as create covalent bonding at the interface of PDMS and NC-PNIPAM; d) Schematic illustrating the folding/unfolding process of the printed NC-PNIPAM/PDMS bilayer structure with an active NC-PNIPAM hinge. The grey substrate and blue hinge represent PDMS and NC-PNIPAM, respectively. w is the hinge width, h_E and h_H are the thickness of PDMS and NC-PNIPAM, respectively. θ is the defined folding angle; e) The real sample in water at 22 °C folds to a certain angle (right) and unfolds to flatten state in a 45 °C water bath (left).

these surface treatment strategies are generally not compatible with the extrusion-based 3D printing method as additional surface treatment steps are required in the interval between printing these two materials. Thus, we directly doped the PDMS precursor with benzophenone to create covalent bonds at the interface of the NC-PNIPAM and the PDMS during UV irradiation (**Figure 1**a). Benzophenone can be excited to singlet state upon absorbing photon, and further convert to triplet state by intersystem crossing (ISC). It then relaxes from the triplet state by abstracting hydrogen atoms from the C-H bonds on the elastomer chains, creating reactive sites for grafting the PNIPAM polymer chain onto the PDMS network (Figure 1b).[45] Thus, covalent bonding is formed to provide adhesion that is strong enough to maintain the structural integrity during the shape deformation of the bilayer structures. To quantify the adhesion strength, we carried out 180° peeling test of the NC-PNIPAM/PDMS bilayer structures. In both NC-PNIPAM (253) and NC-PNIPAM (20) cases, the samples break due to the hydrogels' failure whereas the bilayer part (i.e., adhered part) remains fully intact (Figure S1, Supporting Information). This result indicates that the minimum adhesion strength between NC-PNIPAM hydrogels and PDMS is higher than the maximum tensile stress of NC-PNIPAM hydrogel, which is 14.8 and 17.5 kPa for NC-PNIPAM (253) and NC-PNIPAM (20), respectively.

To enable extrusion-based 3D printing, both PNIPAM and PDMS precursors are formulated to meet the desired rheological properties. First, the NC-PNIPAM precursor ink is composed of NIPAM as a monomer, N,N′-methylenebisacrylamide (BIS) as a crosslinker, Irgacure 2959 as a photoinitiator, and NC as a rheology modifier.[46] The unique "house-of-cards" structure of NC readily turns the liquid-like (loss modulus G'' > storage modulus G') non-printable hydrogel precursor solution to the paste-like ($G' > G''$) printable ink,[47] which exhibits shear thinning behavior to facilitate extrusion during printing and the yield stress of 200 Pa to hold its shape after printing (Figure S2a,b, Video S1, Supporting Information).[48] The PDMS precursor ink is composed of PDMS precursor (Sylgard 184, consisting of 10 wt% crosslinkers), benzophenone as a photoinitiator for creating covalent bonding between NC-PNIPAM and PDMS, and fumed silica nanoparticles (SiNPs) as a rheology modifier. The hydrogen bonding formed within the silanol groups on the SiNPs surface creates a network within the PDMS precursor, which leads to an increase in the G' and viscosity of the inks.[49] As a result, the addition of SiNPs readily transforms the flowable PDMS precursor resin ($G'' > G'$) into a paste-like ink ($G' > G''$) with a yield stress of 100 Pa and endows the ink with shear-thinning behavior (Figure S2c,d, Supporting Information). The as-prepared PDMS precursor ink was loaded into the printing barrel then printed into the desired structures with 10 mm s^{-1} printing speed using a 20 gauge (0.6 mm inner diameter) blunt tip dispensing needle (Figure 1c–i). Because vinyl groups in NIPAM inhibit the curing of PDMS by binding to the platinum catalyst to prevent the crosslinking reaction,[50] PDMS substrates were cured in an oven at 80 °C for 30 min before the printing of NC-PNIPAM precursor ink. Subsequently, the NC-PNIPAM precursor ink was printed as the active hinge on the cured PDMS substrate (Figure 1c-ii) and transferred to cure under UV irradiation (365 nm) after

printing (Figure 1c-iii). Upon immersing the cured hinge-based NC-PNIPAM/PDMS bilayer structures in water at 22 °C (i.e., below the LCST of PNIPAM), the strain mismatch generated between the swellable NC-PNIPAM and the non-swellable PDMS leads to folding. We varied the bilayer structure with different hinge width w (1.2 to 3.6 mm) and PDMS thickness h_E (0.2 to 0.4 mm) to program the folding angle θ in the range of 0 to 180°, while the NC-PNIPAM thickness h_H is fixed to 0.6 mm (Figure 1d). The folding and unfolding process is reversible by the cooling-heating cycle due to the temperature-responsive characteristic of PNIPAM, in which the polymer chains collapse and expel water from its network as the temperature increases above LCST,[51] resulting in a volume shrinkage (*i.e.*, decreased h_H and w), such that the folded structure unfolds to the flat state (Figure 1e). We note that the strong adhesion rendered by the covalent bonding formed between the NC-PNIPAM and PDMS is crucial to the shape morphing. No delamination occurs during the folding and unfolding process up to ten cycles, and the bilayer structures have been maintained their structural integrity for more than eight months so far.

Different UV light intensities were used to tune the microstructure of NC-PNIPAM via different decomposition mechanisms during the photo-crosslinking process. After printing the NC-PNIPAM ink onto the cured PDMS substrate, the hinge-based bilayer structures were exposed to UV irradiation to photo-crosslink NC-PNIPAM with the light intensity of 20 and 253 mW cm^{-2} for 30 min and 2 min 22 s, respectively. The UV dose in these two conditions was fixed to 36 J cm^{-2}. NC-PNIPAM (20) exhibits an obvious phase separation phenomenon with aligned "white dots" along the printing direction (**Figure 2**a), whereas the NC-PNIPAM (253) is transparent throughout the sample (Figure 2b). The inset image of Figure 2b shows a lower magnification image of the same NC-PNIPAM (253) sample to highlight its transparency. To confirm the phase separation of NC-PNIPAM, we freeze-dried NC-PNIPAM (20) and NC-PNIPAM (253) to conduct scanning electron microscopic (SEM) imaging. At the interface between white dots and transparent part within the NC-PNIPAM (20), it is obvious that the transparent part shows a typical hydrogel network with porous microstructure result from the water-to-ice transformation during freezing,[52] whereas the white dots exhibit a much denser network (Figure 2c). In contrast, NC-PNIPAM (253) exhibits a typical hydrogel network with porous microstructure distributed in the entire matrix (Figure 2d). These SEM results indicate that phase separation was induced between PNIPAM and NC during the photo-crosslinking at UV intensity of 20 mW cm^{-2}, in which the white dots are dominated by the aggregated NC clusters (Figure 2e–i), whereas the transparent part is the PNIPAM-rich domain (Figure 2e-ii).

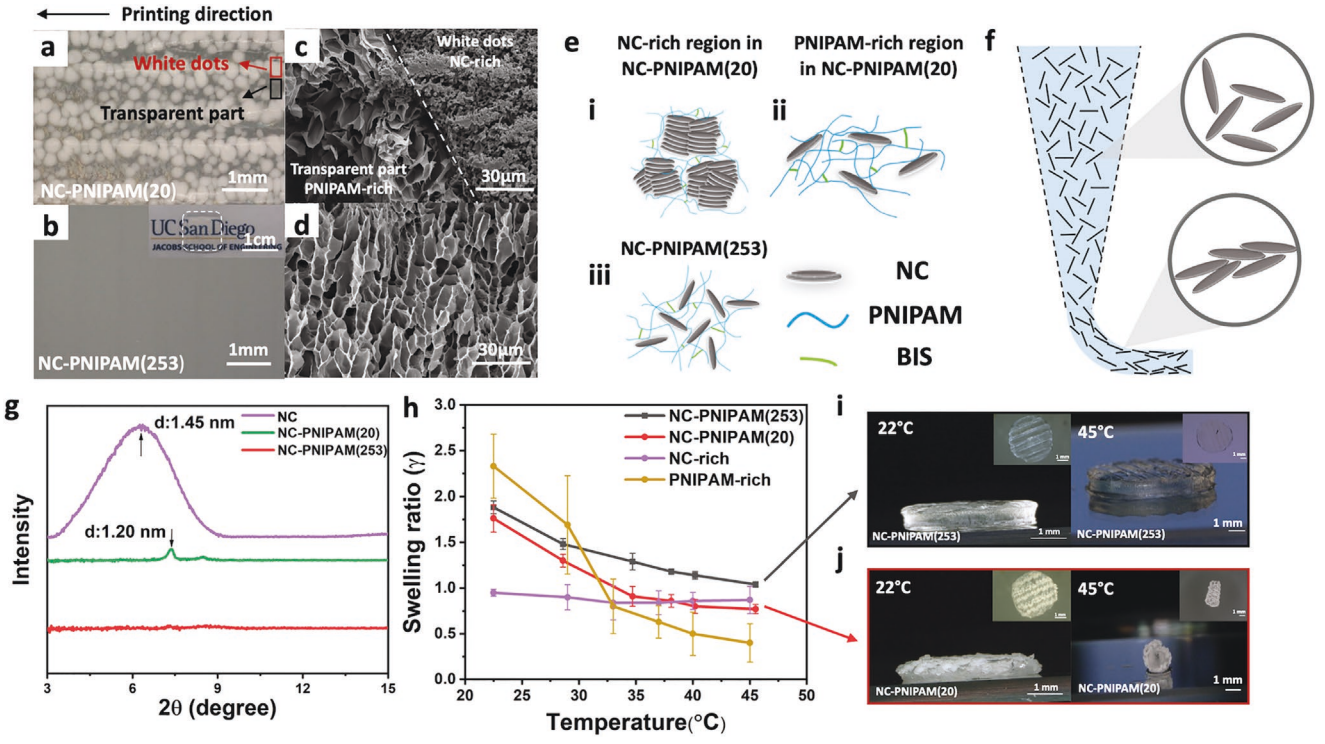

Figure 2. Optical microscope images of a) NC-PNIPAM (20) with the notation of white dots and transparent part, b) NC-PNIPAM (253), inset image is the higher magnification image of the same sample; SEM images of c) the interface of NC-rich region (white dots) and PNIPAM-rich region (transparent) in NC-PNIPAM (20) and d) transparent NC-PNIPAM (253) matrix; e) Schematic of the microphase separation of i, NC-rich region ii, PNIPAM-rich region in NC-PNIPAM (20) and iii, homogeneous microstructure in NC-PNIPAM (253); f) Schematic of shear stress induced alignment of NC during extrusion; g) XRD profile of NC/water suspension, NC-PNIPAM (20) and NC-PNIPAM (253), respectively; h) Plot of temperature dependent swelling of the NC-rich and PNIPAM-rich region in NC-PNIPAM (20), NC-PNIPAM(20) (as a whole) and NC-PNIPAM(253) ($n = 3$); Side and top view (inset image) of i), NC-PNIPAM (253) and j), NC-PNIPAM (20) at as-prepared state (i.e., before swelling) at 22 °C and after de-swelling at 45 °C, respectively. Data are shown as the mean ± SD.

However, in NC-PNIPAM (253) case, the NC discs were well distributed within the NC-PNIPAM (253) matrix (Figure 2e-iii), which is responsible for its transparency. To confirm the alignment of the NC-rich domain, we cured the solution cast sample using the same composition of NC-PNIPAM ink at 20 mW cm^{-2} for 30 min. As a result, randomly distributed NC-rich domains were generated after photo-crosslinking (Figure S3, Supporting Information). Thus, we suspect that the alignment of the NC-rich domain is induced by the shear stress generated by the ink extrusion during the 3D printing process (Figure 2f).[53]

The distinct morphology difference between NC-PNIPAM (20) and NC-PNIPAM (253) is the result of the competition between phase separation and photo-crosslinking kinetics. The light intensity-dependent phase separation has been reported in polymer/monomer mixture systems when the monomer is selectively polymerized and crosslinked, in which nucleation-and-growth was observed at low intensity and spinodal decomposition was observed at high intensity.[10,37] In NC-PNIPAM (20) case, the viscosity change during the polymerization and crosslinking is relatively slow because of the low UV intensity,[54] thus the NC can gradually undergo nucleation-and-growth to reach a global-free-energy minimum driven by decreased entropy and increased elastic free energy as the network is formed.[55–57] In addition, the temperature during polymerization and crosslinking reached about 38 °C at 253 mW cm^{-2}, but the maximum temperature reached about 26 °C at 20 mW cm^{-2} (Figure S4a,b, Supporting Information). We note that not only the strong intensity but also the exothermic reaction of photo-crosslinking contributes to the high temperature (about 38 °C) produced at 253 mW cm^{-2}, which is verified by the control experiment of measuring the water temperature under the UV intensity of 253 and 20 mW cm^{-2}, respectively (Figure S4a,b, Supporting Information). Therefore, the spinodal decomposition is presumably triggered by the UV irradiation at the beginning of polymerization and crosslinking but was suppressed and frozen immediately due to the fast crosslinking kinetics at high temperature and UV intensity.[37] Moreover, the XRD profiles support the abovementioned explanations for the photo-crosslinking induced microphase separation (Figure 2g). The average distance of NC discs decreased from 1.45 to 1.2 nm in NC-PNIPAM (20) compared to the same amount of NC (10 wt%) in water suspension. However, there is no peak found in the XRD profile of NC-PNIPAM (253), indicating NC was homogeneously mixed in the PNIPAM matrix.

To further characterize their temperature-responsive behaviors, linear swelling/de-swelling ratios (γ) were measured at different temperatures ranging from 22 to 45 °C (Figure 2h). To prepare samples for the measurement, the NC-PNIPAM precursor was 3D printed into a $15 \times 15 \times 0.6$ mm square shape and photo-crosslinked at 20 and 253 mW cm^{-2}, respectively. After the NC-PNIPAM hydrogels reach their equilibrium state at 22 °C, the samples were biopsy-punched to disk shape with a diameter of 5 mm (D). γ were calculated using $\gamma = D_T / D_o$ where D_o is the initial diameter measured before swelling/de-swelling in water, and D_T is the diameter measured at temperature T. NC-PNIPAM (253) possesses temperature-responsive size change with $\gamma = 1.9$ and 1.1 at 22 and 45 °C, respectively. Due to its nearly isotropic swelling/de-swelling, the NC-PNIPAM (253) remains flat as its as-prepared state after de-swelling at 45 °C (Figure 2i). As expected, the NC-rich region in NC-PNIPAM (20) serves as a non-swellable component, as the γ is always maintained at nearly 1 across the entire temperature range. In contrast, the PNIPAM-rich region in NC-PNIPAM (20) has a relatively large $\gamma = 2.38$ and 0.40 at 22 °C and 45 °C, respectively. Note that the γ of the entire NC-PNIPAM (20) sample is about the average value of the NC-rich and the PNIPAM-rich regions. Notably, the NC-PNIPAM (20) transforms from a flat to a rolled state after de-swelling at 45 °C (Figure 2j). This is presumably because of the local gradient in the de-swelling ratio between the NC-rich and PNIPAM-rich regions along the thickness direction, where NC-rich regions are mostly located at the top surface of NC-PNIPAM (20) (left photograph of Figure 2j), which serve as a non-deswellable component while the PNIPAM-rich region exhibit significant shrinkage at 45 °C ($\gamma = 0.40$), resulted in the rolling of the NC-PNIPAM(20) disk. Nanoindentation tests were carried out to further study the microscopically localized mechanical properties of NC-PNIPAM hydrogels. The Young's modulus of NC-rich and PNIPAM-rich regions in NC-PNIPAM (20) is 23.97 ± 8.91 and 2.07 ± 0.40 kPa, respectively, whereas NC-PNIPAM (253) has Young's modulus of 11.98 ± 2.57 kPa (Table S1, Supporting Information). Next, we conducted tensile tests to characterize the macroscopic mechanical properties of NC-PNIPAM hydrogels. NC-PNIPAM (20) exhibits anisotropic behaviors as the test samples printed perpendicular to the stretching direction have a smaller Young's modulus of 23.06 ± 2.37 kPa than the ones printed parallel (34.05 ± 2.58 kPa) (Figure S5, Supporting Information). On the other hand, NC-PNIPAM (253) shows similar stress-strain curves no matter printed parallel or perpendicular to the stretching direction, indicating its isotropic behavior. The calculated average Young's moduli are listed in Table S2, Supporting Information, three replicas were tested for each condition. Moreover, NC-PNIPAM (20) possesses a higher elongation at break and toughness than NC-PNIPAM (253) as shown in Figure S5, Supporting Information.

We next examine the influence of microphase separation on the folding actuation speed. The NC-PNIPAM/PDMS bilayer structures were prepared by integrating the PDMS as the passive substrate and either NC-PNIPAM (20) or NC-PNIPAM (253) as the active hinge. Investigations of their unfolding and folding kinetics were carried out by measuring the folding angles (θ) as a function of time at 50 and 22 °C, respectively. The θ of the bilayer sample with a hinge of NC-PNIPAM (253) linearly decreased from 180° to 130° in 60 s with an unfolding speed of 0.8° s^{-1} (**Figure 3**a). Eventually, the NC-PNIPAM (253)/PDMS bilayer sample takes around 60 min to be fully flattened. In contrast, the unfolding speed of the bilayer sample with a hinge of NC-PNIPAM (20) exhibits two different regimes. First, the θ drastically decreases from 180° to 40° within 10 s with an unfolding speed of 14 ° s^{-1}, which is more than one order of magnitude faster than the bilayer structure with NC-PNIPAM (253). Then, the θ reached nearly 0° in 50 s. The corresponding photographs and video visually demonstrate the different de-swelling kinetics of bilayer sample with NC-PNIPAM (20) (left) and NC-PNIPAM (253) (right) (Figure 3b and Video S2, Supporting Information). Similarly, the bilayer sample with NC-PNIPAM (20) also shows a faster folding speed than NC-PNIPAM (253) at 22 °C (Figure 3c). Within 60 s, the

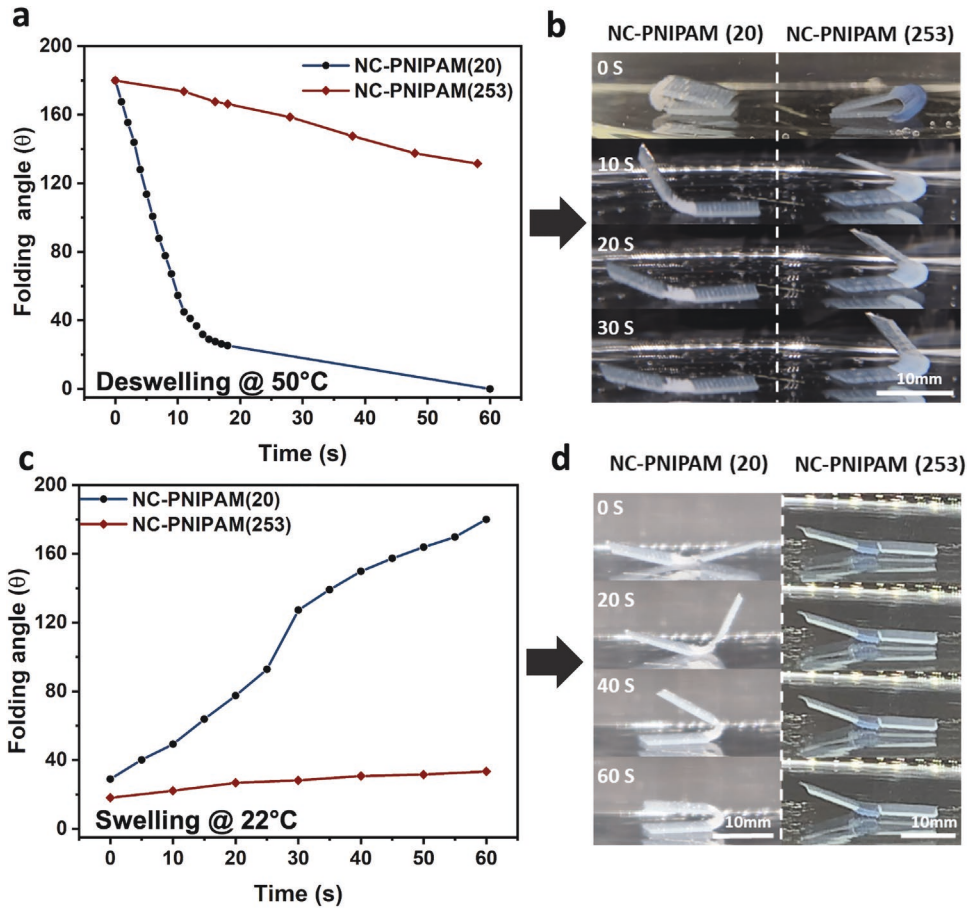

Figure 3. a) De-swelling and c) swelling kinetics of NC-PNIPAM (20) and NC-PNIPAM (253); Photographs showing the different b) de-swelling and d) swelling kinetics for NC-PNIPAM (253) (right) and NC-PNIPAM (20) (left). Both samples are printed with h_H = 0.6 mm, h_E = 0.2 mm, and w = 3.6 mm.

bilayer sample with NC-PNIPAM (20) folds from 28° to 180°, whereas the bilayer sample with NC-PNIPAM (253) has a negligible θ change from 19° to 29° as shown in Figure 3d. We note that the structural parameters (i.e., h_E, h_H, and w) could also influence the folding/unfolding kinetics. For instance, the data shown in Figure 3 are based on h_E = 0.2 mm, h_H = 0.6 mm, and w = 3.6 mm, but increasing h_E and h_H lead to slower folding/unfolding speeds.

The water diffusion in NC-PNIPAM determines the rate of swelling/de-swelling therefore the self-folding actuation speed, and the characteristic time for swelling is proportional to the square of the linear dimension of the hydrogel.[58] Thus, the one order of magnitude faster actuation speed of the bilayer sample with NC-PNIPAM (20) compared to NC-PNIPAM (253) can be attributed to its unique heterogeneous structure and swelling gradient due to the presence of the NC-rich and PNIPAM-rich regions.[59] For the hinge with NC-PNIPAM (253), the in-plane dimensions are more than one order of magnitude larger than the h_H, therefore the water flux is mostly in the thickness direction as the NC-PNIPAM absorb water from its top free surface. This means that the water diffusion rate is dominated by h_H. The diffusivity (D) for PNIPAM has been reported of the order 10^{-11} m^2 s^{-1}.[60] Thus, the characteristic swelling time for NC-PNIPAM (253) is of the order 10^4 s using h_H = 0.6 mm. However, due to the presence of NC-rich domain in NC-PNIPAM (20), the characteristic swelling time can instead be dominated by the size scale between the swellable PNIPAM-rich domain and the non-swellable NC-rich domain, which is ≈100 µm as obtained from Figure 2a. Note that D of NC-PNIPAM (20) and NC-PNIPAM (253) should be the same since they are composed of identical materials. Therefore, the characteristic swelling time for NC-PNIPAM (20) is of the order 10^3 s, which is one order of magnitude faster than NC-PNIPAM (253). This calculated value is consistent with the result we experimentally measured. In addition, the transparent part of NC-PNIPAM (20) possesses an overall larger pore size (3.30 ± 1.61 µm) than that of NC-PNIPAM (253) (1.43 ± 0.49 µm) (pore size obtained based on Figure 2c,d), which can also facilitate the water diffusion. This is probably because NC-PNIPAM (253) has a higher crosslinking density compared to the PNIPAM-rich region in NC-PNIPAM (20), as the homogeneously distributed NC in NC-PNIPAM (253) matrix can serve as a physical crosslinker due to the presence of hydrogen bonding between PNIPAM polymer chains and NC discs.[61]

Next, we demonstrate that the folding angle can be programmed by the geometric parameters of the hinge-based hydrogel/elastomer bilayer structures (**Figure 4**a,b). A series of samples with prescribed w ranging from 1.2 to 3.6 mm, h_E

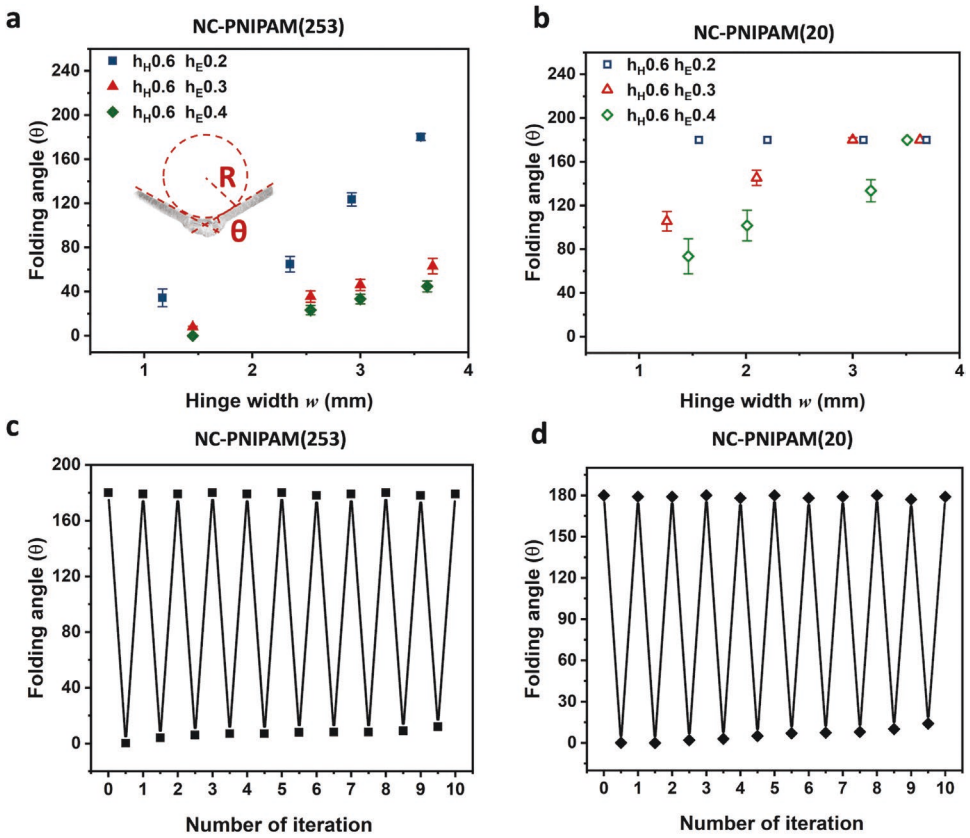

Figure 4. Measured folding angles (θ) of samples with a) NC-PNIPAM (253) and b) NC-PNIPAM (20) as a function of w, with a fixed h_H = 0.6 mm and varied h_E = 0.2 (blue), 0.3 (red), 0.4 mm (green), respectively (n = 3); Cyclic test of samples with c) NC-PNIPAM (253) and d) NC-PNIPAM (20), θ were measured over 10 cycles. Data are shown as the mean ± SD.

ranging from 0.2 to 0.4 mm, and h_H = 0.6 mm were prepared by the 3D-extrusion printing and photo-crosslinking process, followed by immersing the samples in DI water for 24 h at 22 °C to let NC-PNIPAM hinges swell to its equilibrium state. The folding angles were measured using an optical microscope, three replicas were measured for each condition. For a given h_E, the θ increase linearly with the w until it reaches 180°, indicating that the radius of curvature (R) is constant across the entire w, thus θ follows the formula of $\theta = w/R$. Whereas for a given w, θ decreased with increasing h_E and fixed h_H = 0.6 mm (Figure 4a,b). Moreover, the θ for samples with NC-PNIPAM (20) hinges are larger than that of NC-PNIPAM (253) using identical geometric parameters. The calculated angle using the Timoshenko model has been found to agree reasonably well with the θ measured experimentally. We note that the Timoshenko model implies that the normalized curvature R/h_H would remain constant as long as h_E/h_H remains the same within the same material system. To illustrate this point as well as examine the influence of hydrogel thickness on θ, we fabricated a set of samples with h_H = 0.4 mm, h_E = 0.2 mm, and w ranging from 1.3 to 3.8 mm then measured their θ as a function of w (Figure S6, Supporting Information). As expected, for samples with NC-PNIPAM (253) hinges, θ exhibits a positive linear relationship with w (i.e., $\theta = w/R$). For samples with NC-PNIPAM(20) hinges, θ increases as the increasing of w until it reached 180°. Importantly, the differences in the experimentally measured R/h_H between samples with different h_H (0.4 vs. 0.6 mm) but similar $h_E/h_H \approx 0.5$ are less than 4.4 and 0.9% for samples with NC-PNIPAM (253) and NC-PNIPAM (20) hinges, respectively, which are consistent with the conclusion drawn from Timoshenko model (Figure S7, Supporting Information). The detailed folding mechanism and calculation are discussed in the Supporting Information. The temperature cycles between 22 and 45 °C are repeated 10 times to demonstrate the reversibility of folding-unfolding, θ for the bilayer structure with NC-PNIPAM (253) and NC-PNIPAM (20) hinges were measured and plotted in Figure 4c,d, respectively. The time interval for each measurement point was set to 12 h to ensure the NC-PNIPAM reach the equilibrium state. A trivial hysteresis (≈7°) was found at the de-swelling state after 10 cycles. We suspect this is due to the plastic deformation of the PDMS substrate.

To further demonstrate the different folding kinetics of the bilayer structures with hinges of NC-PNIPAM (20) and NC-PNIPAM (253), we design and print a structure with double hinges of NC-PNIPAM (20) on the left and NC-PNIPAM (253) on the right as the schematic shown in **Figure 5**a. Identical structural parameters (h_H = 0.6 mm, h_E = 0.2 mm, and w = 4 mm) were used to directly compare the folding/unfolding speeds. The series of photographs showing folding and unfolding during a cooling-heating cycle (22—50 °C) clearly illustrate that the hinge with NC-PNIPAM (20) folds significantly faster than

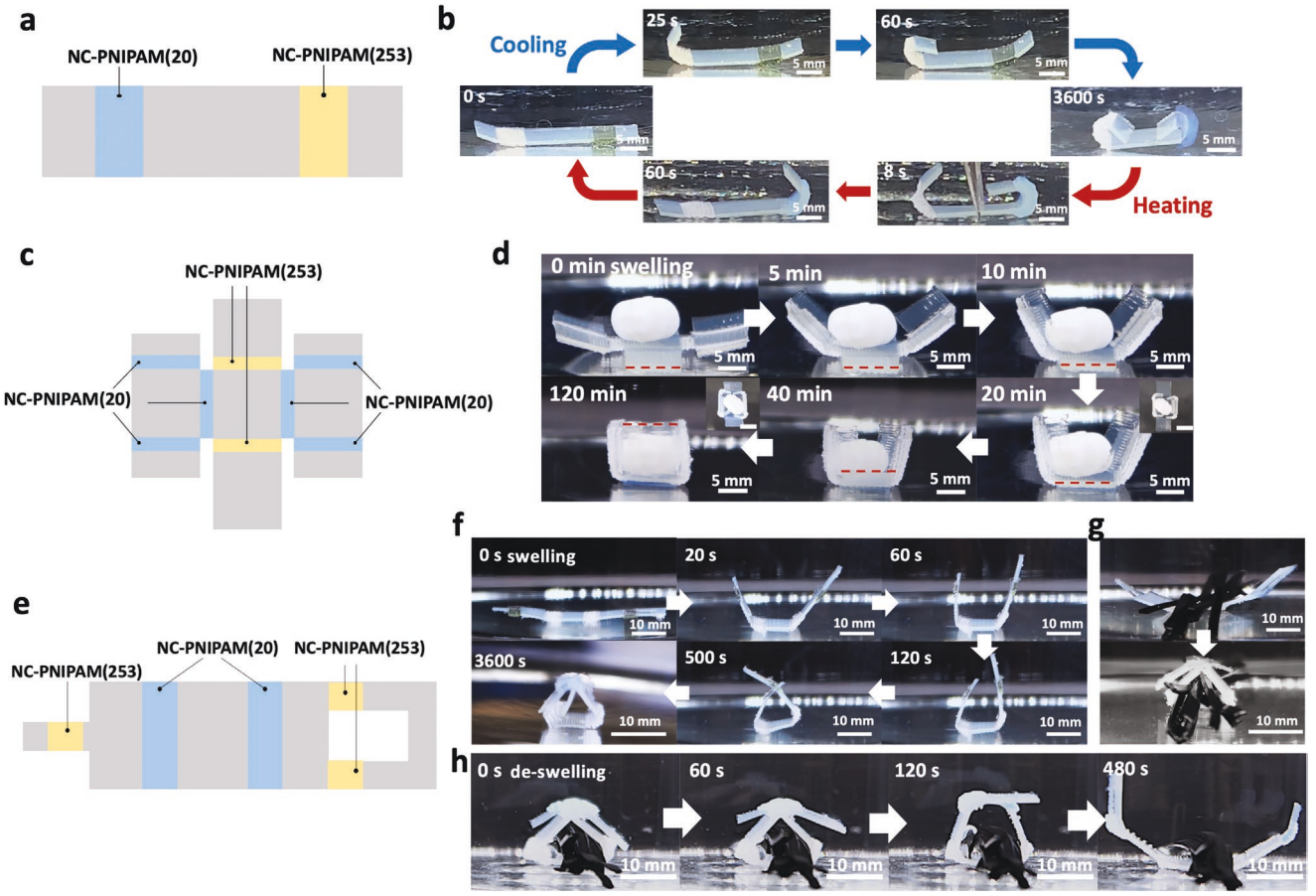

Figure 5. Sequential folding structure demonstration. a) Schematic and b) photographs of the sequential self-folding structure with double hinges during cooling and heating cycle at 22 °C and 45 °C, respectively; c) Schematic of the box structure with flaps; d) Photographs of the sequential folding box structure capturing a small round object (diameter ≈ 10 mm) during swelling at 22°C, the inset images are top views of the same sample, scale bar = 10 mm. The red dash line indicated the edge of the front pad; e) Schematic of the self-locking latch structure; f) photographs of the self-locking latch structure during swelling at 22 °C; Demonstration of g) capturing and h) releasing plastic strips during the swelling at 22 °C and deswelling at 45 °C, respectively, using the self-locking latch structure.

the one with NC-PNIPAM (253), as it completely folds from 0° to 180° within 60 s upon cooling (Figure 5b). However, the hinge with NC-PNIPAM (253) reaches 180° after 3600 s. Subsequently, this structure with double hinges was immersed in a 50 °C water bath to de-swell. Similar to the folding process, the hinge with NC-PNIPAM (20) exhibits much faster unfold kinetics than the one with NC-PNIPAM (253) (Video S3, Supporting Information). We exploited such distinct folding and unfolding speed offered by the different swelling/de-swelling kinetics of NC-PNIPAM to realize the formation of a structure that requires sequential folding, for example, a box and a self-locking latch structure. The box structure with flaps is widely used in packaging to store items more securely. This kind of structure requires a two-stage folding sequence to properly self-assemble into the box structure. Thus, we assign two middle hinges to NC-PNIPAM (253) and the other side hinges to NC-PNIPAM (20) (Figure 5c). According to the relationship between θ and structural parameters we explored in Figure 4a,b, we set $h_H = 0.6$ mm, $h_E = 0.4$ mm, $w = 1.8$ mm for NC-PNIPAM (20), and $h_H = 0.6$ mm, $h_E = 0.2$ mm, $w = 2.4$ mm for NC-PNIPAM (253) to achieve the θ at 90°. After immersing the box structure at 22 °C water bath, the hinges with NC-PNIPAM (20) fold first due to the faster swelling kinetics, which takes about 20 min for them to reach 90°. Finally, as the NC-PNIPAM (253) slowly swells to its equilibrium state, the box structure can be assembled and capture the round object inside (diameter ≈ 10 mm) (Figure 5d). We adopt the self-locking structures that have been shown before to demonstrate the controlled self-folding process (Figure 5e). [22,25] We assign two middle hinges to NC-PNIPAM (20) (blue) and the three side hinges to NC-PNIPAM (253) (yellow). A rectangular void is designed on the right end of the panel and a protruded rectangular shape is designed on the left end panel. Once the structure is immersed in a 22 °C water bath, the faster swelling kinetics of NC-PNIPAM (20) leads the middle panels to fold first, letting the protruded rectangular panel on the left go through the void (Figure 5f). Finally, this structure can lock itself as the hinges with NC-PNIPAM (253) slowly fold until it swells to the equilibrium. Such structures are useful to capture and hold the target object securely. Here, we demonstrate the ability to collect and tighten a bunch of plastic strips using the self-locking structure as a proof-of-concept (Figure 5g, Video S4, Supporting Information).

We note that the captured object can be further released by de-swelling the NC-PNIPAM, and the releasing speed is governed by the de-swelling kinetics of NC-PNIPAM (253) (Figure 5h, Video S5, Supporting Information).

3. Conclusions

In summary, we have developed a strategy to enable sequential and reversible self-folding without changing the chemical composition or structural dimensions when subjected to a globally applied static stimulus. Both the NC-PNIPAM and PDMS precursor inks are formulated not only to fulfill the rheological requirements for extrusion-based 3D printing with sub-millimeter printing resolution but also to achieve good adhesion between NC-PNIPAM hinges and PDMS substrates. We have also demonstrated that different swelling/de-swelling kinetics of NC-PNIPAM, which determine its folding kinetics, can be achieved by the UV intensity-dependent phase separation through nucleation-and-growth during photo-crosslinking. Such phase-separated microstructures led to more than one order of magnitude faster folding speed compared to the one with the same chemical composition but nearly homogenous microstructure. We then designed and printed bilayer structures with programmable folding angles and sequential folding capabilities to demonstrate capturing, holding and fastening objects. We anticipate that our study will open new routes to encode the specific responsiveness of nanocomposite hydrogel-based systems in terms of shapes and speeds by controlling their internal microstructures and geometrical design to autonomously complete specific tasks.

4. Experimental Section

Materials: N-isopropylacrylamide (NIPAM, stabilized with 4-methoxyphenol, M_W = 113.16 g mol^{-1}) was purchased from Tokyo Chemical Industry (TCI) America. PDMS (Sylgard 184) was purchased from Dow Corning. N,N′-methylenebisacrylamide (BIS), Irgacure 2959, benzophenone, and (Tridecafluoro-1,1,2,2 Tetrahydrooctyl) dimethylchlorosilane (silane) were purchased from Sigma-Aldrich(St Louis, MO, USA). Acetone and isopropyl alcohol were purchased from Fisher Scientific. Silica nanoparticles (SiNPs, CAB-O-SIL EH-5) were purchased from Cabot Corporation. Nanoclay (NC, Laponite-RD) was obtained by BYK Additives & Instruments. All chemicals were used as received without further purification.

Preparation of PDMS Precursor Ink: The PDMS precursor inks were prepared by a simple one-pot mixing process containing PDMS base/crosslinker (10:1), benzophenone (1.8 wt.% with respect to PDMS base), and SiNPs (15 wt.% with respect to PDMS base) in a Thinky planetary mixer (Thinky U.S.A., Inc.) mixing at 2000 rpm for 3 min and followed by degas process at 2000 rpm for 2 min to remove any air bubbles. Since benzophenone is in the solid-state at room temperature, in order to achieve better mixing quality, it was heated in an oven at 70 °C for 10 min to melt before adding to PDMS precursor. After mixing, the inks were loaded into a 10 mL syringe (Fisher Scientific) and centrifuged at 4000 rpm for 20 min to eliminate any air bubbles.

Preparation of NC-PNIPAM Precursor Ink: NIPAM solution (2 M) and BIS solution (0.13 M) were prepared by adding NIPAM and BIS to deionized (DI) water respectively and mixed by vortex mixer until all chemicals dissolve at room temperature. Then NIPAM solution (10 mL, 2 M), BIS solution (120 µL, 0.13 M), Irgacure 2959 (0.04 g) and NC (1 g) were added into a 35 mL container (Thinky U.S.A., Inc.) and mixed at 2000 rpm for 5 min or longer time until it was mixed well with no visible NC aggregates. Finally, the mixed ink was loaded into a 10 mL syringe (Fisher Scientific) and centrifuged at 2000 rpm for 10 min to eliminate any air bubbles.

Preparation of Silane-Treated Glass Slides: Glass slides were used as substrates during the 3D printing process after treating with silane to eliminate any residual stress generated during the peeling procedure. First, untreated glass slides (75 mm × 50 mm × 1 mm) were cleaned using acetone and dried by air blowing. The cleaned glass slides were then transferred to a desiccator, 2 drops of silane were transferred onto one glass substrate as a reservoir using a glass pipet. The desiccator was vacuumed using a pump for 12 h to make silane treated glass slides, after that, the silane treated glass slides were taken out, washed with isopropyl alcohol, and stored in a petri dish sealed with parafilm for further use.

Extrusion-Based 3D Printing and Fabrication: PDMS/NC-PNIPAM bilayer structures were fabricated by direct ink writing using a 3D printer (Rokit, Invivo). The 10 mL syringe stored with PDMS precursor ink was placed in the extrusion carriage of the 3D printer and printed on a silane treated glass slide using a 20-gauge blunt tip dispensing needle at 0.003 mL s^{-1} deposition rate (0.6 mm inner diameter). The printed PDMS substrate with hinge structure was cured in an oven at 80 °C for 30 min. After that, NC-PNIPAM precursor ink was directly printed on the hinge section of the cured PDMS substrate at 0.005 mL s^{-1} deposition rate, the printed bilayer structure was then transferred into a homemade transparent humid box to prevent NC-PNIPAM drying out while UV irradiation (365 nm). To fabricate NC-PNIPAM with different microstructures, different UV intensities were applied while keeping the constant UV does. NC-PNIPAM (20) and NC-PNIPAM (253) were cured with UV intensity of 20 mW cm^{-2} for 30 min (UV source provided by JAXMAN) and of 253 mW cm^{-2} for 2 min and 22 s (UV source provided by Omnicure), respectively.

Characterization: Stress-strain data of tensile test and 180° peeling test were obtained using a universal testing machine (Instron Corp., Instron 5982) with a strain rate of 10 mm s^{-1}. For a tensile test, rectangular strips (35 × 8 × 0.8 mm as-prepared) of NC-PNIPAM (20) and NC-PNIPAM (253) were printed parallel and perpendicular to the stretching direction while tensile tests, respectively. The tensile test was carried out after the samples reached their equilibrium swelling states at 22 °C. For the 180° peeling test, the samples were fabricated by placing a tape in between the cured PDMS and the printed NC-PNIPAM precursor to separate these two materials such that after photo-crosslinking, the region with the tape does not have adhesion whereas the region where NC-PNIPAM contacts with the PDMS has covalent bonding. The contact region (i.e., bilayer) has an as-prepared dimension of 20 × 8 × 1.2 mm. The 180° peeling tests were carried out after the samples reached their equilibrium swelling state at 22 °C. Localized Young's modulus of NC-PNIPAM hydrogels was characterized by Nanoindenter (OPTICS, PIUMA). The NC-PNIPAM hydrogels were first swelling in DI water at 22 °C for at least 48 h to reach their equilibrium state. Then samples were biopsy-punched to a disk shape with 5 mm diameter and 0.8–1.2 mm thickness. The average values of Yong's modulus for each condition were calculated based on 3 samples. Rheological data was obtained using an ARG2 rheometer by TA instruments. The viscosity measurements were set to a steady-state with a shear rate ranging from 0.1 to 100 s^{-1}. The modulus measurements were set to an oscillatory state with a shear rate ranging from 0.1 to 1000 s^{-1}. Optical micrographs were captured using an optical microscope (Keyence VHX1000). Images of the microporous structure were obtained using scanning electron microscopic (SEM) imaging (FEI Quanta FEG 250). X-ray diffraction (XRD) profiles were performed using Cu X-rays (λ = 1.54 Å) with 2θ range from 3° to 50° in a step of 0.02° with 0.5 s dwell. (Bruker D8 Advanced equipped with a LynxEye CCD detector)

Statistical Analysis: All data were expressed as mean ± standard deviation (SD). A minimum of three tests were performed for nanoindentation, tensile test, swelling ratio and folding angle measurement to ensure that reported results were significant.

Supporting Information

Supporting Information is available from the Wiley Online Library or from the author.

Acknowledgements

This work was supported by the National Science Foundation through the University of California San Diego Materials Research Science and Engineering Center (UCSD MRSEC), grant number DMR-2011924. The authors would like to thank Booseong Kim for helpful discussions about the adhesion between hydrogels and elastomers.

Conflict of Interest

The authors declare no conflict of interest.

Data Availability Statement

The data that support the findings of this study are available from the corresponding author upon reasonable request.

Keywords

3D printing, nanocomposite hydrogels, phase separation, sequential folding, soft actuators

Received: January 6, 2022
Revised: February 28, 2022
Published online:

[1] H. Kobayashi, M. Daimaruya, J. F. V. Vincent, in *IUTAM-IASS Symp. on Deployable Structures: Theory and Applications*, Springer, Dordrecht **2000**.
[2] F. Haas, R. J. Wootton, *Proc. R. Soc. London, Ser. B* **1996**, *263*, 1651.
[3] J. W. Kelly, W. E. Balch, *Nat. Chem. Biol.* **2006**, *2*, 224.
[4] J. Ryu, M. Mohammadifar, M. Tahernia, H.-i. Chun, Y. Gao, S. Choi, *Adv. Mater. Technol.* **2020**, *5*, 1901054.
[5] K. Kuribayashi, K. Tsuchiya, Z. You, D. Tomus, M. Umemoto, T. Ito, M. Sasaki, *Mater. Sci. Eng., A* **2006**, *419*, 131.
[6] S. Sundaram, D. S. Kim, M. A. Baldo, R. C. Hayward, W. Matusik, *ACS Appl. Mater. Interfaces* **2017**, *9*, 32290.
[7] S. Felton, M. Tolley, E. Demaine, D. Rus, R. Wood, *Science* **2014**, *345*, 644.
[8] Y. Liu, J. K. Boyles, J. Genzer, M. D. Dickey, *Soft Matter* **2012**, *8*, 1764.
[9] A. Kotikian, R. L. Truby, J. W. Boley, T. J. White, J. A. Lewis, *Adv. Mater.* **2018**, *30*, 1706164.
[10] N. Kimura, K. Kawazoe, H. Nakanishi, T. Norisuye, Q. Tran-Cong-Miyata, *Soft Matter* **2013**, *9*, 8428.
[11] J. Hu, H. Meng, G. Li, S. I. Ibekwe, *Smart Mater. Struct.* **2012**, *21*, 053001.
[12] C. Li, G. C. Lau, H. Yuan, A. Aggarwal, V. L. Dominguez, S. Liu, H. Sai, L. C. Palmer, N. A. Sather, T. J. Pearson, D. E. Freedman, P. K. Amiri, M. O. de la Cruz, S. I. Stupp, *Sci. Rob.* **2020**, *5*.
[13] C. Li, G. C. Lau, H. Yuan, A. Aggarwal, V. L. Dominguez, S. Liu, H. Sai, L. C. Palmer, N. A. Sather, T. J. Pearson, D. E. Freedman, P. K. Amiri, M. O. de la Cruz, S. I. Stupp, *Sci. Rob.* **2020**, *5*, eabb9822.
[14] A. S. Gladman, E. A. Matsumoto, R. G. Nuzzo, L. Mahadevan, J. A. Lewis, *Nat. Mater.* **2016**, *15*, 413.
[15] A. Richter, G. Paschew, S. Klatt, J. Lienig, K.-F. Arndt, H.-J. P. Adler, *Sensors* **2008**, *8*, 561.
[16] S. Chatterjee, P. C. Hui, *Polymers (Basel)* **2021**, *13*, 2086.
[17] R. Marcombe, S. Cai, W. Hong, X. Zhao, Y. Lapusta, Z. Suo, *Soft Matter* **2010**, *6*, 784.
[18] J. Zhang, X. Zhao, Z. Suo, H. Jiang, *J. Appl. Phys.* **2009**, *105*, 093522.
[19] X. Hu, C. Spille, M. Schlüter, I. Smirnova, *Ind. Eng. Chem. Res.* **2020**, *59*, 19458.
[20] A. B. Baker, S. R. G. Bates, T. M. Llewellyn-Jones, L. P. B. Valori, M. P. M. Dicker, R. S. Trask, *Mater. Des.* **2019**, *163*, 107544.
[21] J.-H. Na, A. A. Evans, J. Bae, M. C. Chiappelli, C. D. Santangelo, R. J. Lang, T. C. Hull, R. C. Hayward, *Adv. Mater.* **2015**, *27*, 79.
[22] B. An, S. Miyashita, A. Ong, M. T. Tolley, M. L. Demaine, E. D. Demaine, R. J. Wood, D. Rus, *IEEE Trans. Rob.* **2018**, *34*, 1409.
[23] E. Iwase, I. Shimoyama, in 18th IEEE International Conference on Micro Electro Mechanical Systems, Miami Beach, FL, USA, 30 January–3 February **2005**.
[24] Y. Liu, B. Shaw, M. D. Dickey, J. Genzer, *Sci. Adv.* **2017**, *3*, e1602417.
[25] C. Dai, L. Li, D. Wratkowski, J.-H. Cho, *Nano Lett.* **2020**, *20*, 4975.
[26] S. M. Felton, M. T. Tolley, B. Shin, C. D. Onal, E. D. Demaine, D. Rus, R. J. Wood, *Soft Matter* **2013**, *9*, 7688.
[27] Y. Liu, M. Miskiewicz, M. J. Escuti, J. Genzer, M. D. Dickey, *J. Appl. Phys.* **2014**, *115*, 204911.
[28] J. M. M. Arda Kotikian, E. C. Davidson, R. D. Weeks, C. Daraio, J. A. Lewis, C. McMahan, *Sci. Rob. 4*, **2019**, eaax7044.
[29] A. B. Baker, D. F. Wass, R. S. Trask, *Smart Mater. Struct.* **2016**, *25*, 10LT02.
[30] Y. Mao, K. Yu, M. S. Isakov, J. Wu, M. L. Dunn, H. J. Qi, *Sci. Rep.* **2015**, *5*, 13616.
[31] Y. Lee, H. Lee, T. Hwang, J.-G. Lee, M. Cho, *Sci. Rep.* **2015**, *5*, 16544.
[32] C. Liu, J. Schauff, D. Joung, J.-H. Cho, *Adv. Mater. Technol.* **2017**, *2*, 1700035.
[33] F. Wang, P. Altschuh, L. Ratke, H. Zhang, M. Selzer, B. Nestler, *Adv. Mater.* **2019**, *31*, 1806733.
[34] W. Y. Hsu, S. Wu, *Polym. Eng. Sci.* **1993**, *33*, 293.
[35] G. Yu, J. Gao, J. C. Hummelen, F. Wudl, A. J. Heeger, *Science* **1995**, *270*, 1789.
[36] Q. Tran-Cong-Miyata, H. Nakanishi, *Polym. Int.* **2017**, *66*, 213.
[37] Y. Ochi, R. Kawakubo, D.-T. Van-Pham, Y. Kitamura, H. Nakanishi, T. Norisuye, Q. Tran-Cong-Miyata, *Adv. Nat. Sci. Nanosci. Nanotechnol.* **2015**, *6*, 045002.
[38] I. A. Zucchi, C. E. Hoppe, M. J. Galante, R. J. J. Williams, M. A. López-Quintela, L. Matějka, M. Slouf, J. Pleštil, *Macromolecules* **2008**, *41*, 4895.
[39] Y. Zhang, Y. Shen, K. Shi, T. Wang, E. Harkin-Jones, *Composites, Part A* **2018**, *110*, 62.
[40] S. Fujishige, K. Kubota, I. Ando, *J. Phys. Chem.* **1989**, *93*, 3311.
[41] S. Ma, Y. Zhang, M. Wang, Y. Liang, L. Ren, L. Ren, *Sci. China Technol. Sci.* **2020**, *63*, 532.
[42] J. C. McDonald, D. C. Duffy, J. R. Anderson, D. T. Chiu, H. Wu, O. J. A. Schueller, G. M. Whitesides, *Electrophoresis* **2000**, *21*, 27.
[43] H. Yuk, T. Zhang, G. A. Parada, X. Liu, X. Zhao, *Nat. Commun.* **2016**, *7*, 12028.
[44] C. Cha, E. Antoniadou, M. Lee, J. H. Jeong, W. W. Ahmed, T. A. Saif, S. A. Boppart, H. Kong, *Angew. Chem., Int. Ed.* **2013**, *52*, 6949.
[45] M. H. Schneider, Y. Tran, P. Tabeling, *Langmuir* **2011**, *27*, 1232.
[46] Y. Jin, C. Liu, W. Chai, A. Compaan, Y. Huang, *ACS Appl. Mater. Interfaces* **2017**, *9*, 17456.
[47] K. Haraguchi, T. Takehisa, *Adv. Mater.* **2002**, *14*, 1120.
[48] P. T. Smith, A. Basu, A. Saha, A. Nelson, *Polymer* **2018**, *152*, 42.
[49] J.-N. Paquien, J. Galy, J.-F. Gérard, A. Pouchelon, *Colloids Surf. A* **2005**, *260*, 165.

[50] F. Faglioni, M. Blanco, W. A. Goddard, D. Saunders, *J. Phys. Chem. B* **2002**, *106*, 1714.
[51] K. N. Plunkett, X. Zhu, J. S. Moore, D. E. Leckband, *Langmuir* **2006**, *22*, 4259.
[52] H.-W. Kang, Y. Tabata, Y. Ikada, *Biomaterials* **1999**, *20*, 1339.
[53] C. Zhao, P. Zhang, J. Zhou, S. Qi, Y. Yamauchi, R. Shi, R. Fang, Y. Ishida, S. Wang, A. P. Tomsia, M. Liu, L. Jiang, *Nature* **2020**, *580*, 210.
[54] D. Nwabunma, H.-W. Chiu, T. Kyu, *Macromolecules* **2000**, *33*, 1416.
[55] B. Ruzicka, E. Zaccarelli, L. Zulian, R. Angelini, M. Sztucki, A. Moussaïd, T. Narayanan, F. Sciortino, *Nat. Mater.* **2011**, *10*, 56.
[56] Q. Tran-Cong, A. Harada, *Phys. Rev. Lett.* **1996**, *76*, 1162.
[57] D. Nwabunma, H.-W. Chiu, T. Kyu, *J. Chem. Phys.* **2000**, *113*, 6429.
[58] T. Tanaka, D. J. Fillmore, *J. Chem. Phys.* **1979**, *70*, 1214.
[59] R. Khodambashi, Y. Alsaid, R. Rico, H. Marvi, M. M. Peet, R. E. Fisher, S. Berman, X. He, D. M. Aukes, *Adv. Mater.* **2021**, *33*, 2005906.
[60] J. Yoon, S. Cai, Z. Suo, R. C. Hayward, *Soft Matter* **2010**, *6*, 6004.
[61] X. Di, C. Hang, Y. Xu, Q. Ma, F. Li, P. Sun, G. Wu, *Mater. Chem. Front.* **2020**, *4*, 189.